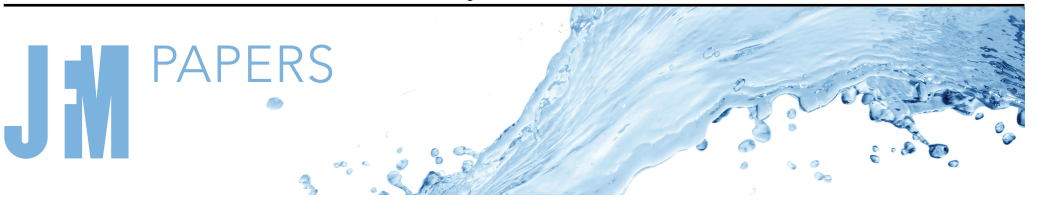
J. Fluid Mech. (2026), *vol.* 1040, A53, doi:10.1017/jfm.2026.11909



Structures of elastoinertial turbulence in pipe flow

Manish Kumar[1,2] **and Michael D. Graham**[1]

[1]Department of Chemical and Biological Engineering, University of Wisconsin-Madison, 1415 Engineering Dr, Madison, WI 53706, USA

[2]National Center for Supercomputing Applications, University of Illinois Urbana-Champaign, Urbana, IL 61801, USA

Corresponding author: Manish Kumar, mkumar48@illinois.edu; manish030297@gmail.com

(Received 23 January 2026 UTC; revised 12 May 2026 UTC; accepted 3 July 2026 UTC)

Elastoinertial turbulence (EIT) is a self-sustaining chaotic state resulting from the interplay between inertia and elasticity in the flow of dilute polymeric solutions, and its emergence is believed to limit the achievable drag reduction in turbulence flow using polymer additives. In the present study, we introduce a viscoelastic variant of spectral proper orthogonal decomposition (VESPOD) that decomposes velocity and polymeric stress fields of EIT together into well-defined orthogonal oscillating modes such that the decomposition is optimal in terms of the total mechanical energy of the flow. Using this technique, we investigate the dominant coherently evolving structures underlying the dynamics of EIT in axisymmetric pipe flow. By analysing distinct peaks in the leading eigenvalue of the VESPOD eigenvalue spectrum, we find that the dynamics of EIT in pipe flow is dominated by three distinct families of travelling waves, where the higher wavenumber structures of each family are simple harmonics of their respective fundamental waves. The radial velocity fields of the travelling waves are characterised by the formation of large-scale structures spanning the pipe radial direction. However, the polymeric stress fields corresponding to them are characterised by the formation of thin inclined sheets of high stress fluctuations at the critical layers of the respective waves, i.e. the locations where the wave speed of the VESPOD mode matches the mean streamwise velocity. Additionally, these sheets exhibit nested structures, where the polymeric sheets of faster waves are confined by those of the immediately slower waves.

Key words: pipe flow, turbulence simulation, viscoelasticity

© The Author(s), 2026. Published by Cambridge University Press. This is an Open Access article, distributed under the terms of the Creative Commons Attribution licence (https://creativecommons.org/licenses/by/4.0/), which permits unrestricted re-use, distribution and reproduction, provided the original article is properly cited.

https://doi.org/10.1017/jfm.2026.11909 Published online by Cambridge University Press

1. Introduction

The reduction of turbulent drag using polymer additives has been an active area of research due to its application to save energy during liquid transport (Xi 2019) ever since it was discovered that the addition of a tiny amount ($\sim O(10)$ ppm) of high molecular weight polymer suppresses inertial turbulence and dramatically reduces frictional drag (Toms 1949). Although polymer additives can significantly reduce frictional drag, the flow does not become laminar; hence the drag is always higher than the laminar value. This phenomenon is attributed to the presence of a self-sustaining weakly fluctuating flow state known as the maximum drag reduction (MDR) asymptote (Virk *et al.* 1970). At MDR, the frictional drag is nearly independent of the type and concentration of polymers; understanding MDR is an important area of research because it sets a limit for the attainable amount of drag reduction. Earlier studies of MDR mainly focused on the ensemble statistics of the velocity fluctuations; however, recent advancements in the field attempt to understand the dynamic evolution of the MDR state (Xi 2019). The discovery of elastoinertial turbulence (EIT), a self-sustaining chaotic state resulting from the interplay between inertia and elasticity, provides some understanding of the dynamics of the MDR state (Samanta *et al.* 2013; Datta *et al.* 2022; Dubief *et al.* 2023). In this paper, we investigate the dynamics of EIT in pipe flow, and discover dominant structures underlying its dynamics.

The EIT can sustain in the parameter regime characterised by the Reynolds number Re (a dimensionless number representing the ratio of inertial to viscous forces) and the Weissenberg number Wi (the product of polymer relaxation time and characteristic strain rate), where the flow is linearly stable, suggesting a nonlinear route for transition to EIT. Viscoelastic two-dimensional (2-D) channel flow becomes linearly unstable due to a wall mode instability at sufficiently large Re (Zhang *et al.* 2013) and a centre mode instability at large Wi (Page *et al.* 2020; Khalid *et al.* 2021), with parameter values significantly higher than the EIT parameter regime of interest here. The wall mode instability leads to the emergence of a travelling wave known as the Tollmien–Schlichting (TS) wave (Drazin & Reid 1981), and the centre mode instability leads to the emergence of another distinct travelling wave having an 'arrowhead' structure (Page *et al.* 2020). The origins of these travelling waves are highly subcritical, and they can persist subcritically to the parameter regimes relevant to EIT. Inspired by these facts, it was speculated that the nonlinear excitation of either the wall mode (Shekar *et al.* 2019, 2020, 2021) or the centre mode (Page *et al.* 2020; Dubief *et al.* 2022) could lead to EIT in two dimensions. Recent advancements indicate that in the elastoinertial regime, wall mode structures dominate the dynamics (Beneitez *et al.* 2024*a*; Kumar & Graham 2024; Kumar *et al.* 2025), while at vanishing Re, the dynamics tends to be organised around the centre mode structures (Morozov 2022; Beneitez *et al.* 2024*b*; Lewy & Kerswell 2025).

Recently, using spectral proper orthogonal decomposition (SPOD) (Towne *et al.* 2018), we have revealed the dominant coherent structures underlying the dynamics of EIT in 2-D channel flow (Kumar & Graham 2024). The SPOD is a temporal variant of proper orthogonal decomposition (POD) (Holmes *et al.* 2012), and decomposes time-dependent state variables into oscillating orthogonal basis functions such that the basis functions are coherent in both space and time. We demonstrated that the dynamics of EIT in channel flow is predominantly composed of a family of non-harmonic travelling waves, where the most dominant travelling wave of the family resembles the structure of the TS wave (Kumar & Graham 2024). The wall-normal velocity of the most dominant travelling wave has large-scale regular structures spanning the channel height, the streamwise velocity

https://doi.org/10.1017/jfm.2026.11909 Published online by Cambridge University Press

component has regular structures in the vicinity of the channel walls, and the polymeric stress field contains thin sheets of high polymeric stress fluctuations localised at the critical layers of the travelling wave. The critical layer is the location where the wave speed of the travelling wave matches the mean streamwise velocity. The remaining travelling waves of the family exhibit similar structures, but nested in the region bounded by the polymeric sheets, hence critical layers of the immediately slower travelling wave. The sheets of high polymeric stress act as barriers for flow and hence prevent velocity fluctuations from penetrating them (Kumar *et al.* 2023). Thus the dynamics of EIT in channel flow originates from a nonlinear excitation of a wall mode, and is dominated by a family of self-similar nested travelling waves where the polymeric sheets of each travelling wave confine the velocity fluctuations of their immediate faster wave. Strengthening the notion of the connection of EIT with wall mode, it has also been found that the arrowhead structure resulting from the centre mode instability is disconnected from EIT, and it does not play a role in the self-sustenance of the dynamics of EIT (Beneitez *et al.* 2024*a*).

The numerical investigation of the dynamics of EIT in pipe flow has received relatively little attention (Lopez *et al.* 2019) and is the topic of the present study. Similar to channel flow, the centre mode becomes linearly unstable even in viscoelastic pipe flow at $Re = O(100)$ and $Wi = O(10)$ (Garg *et al.* 2018; Chaudhary *et al.* 2021). Weakly nonlinear analysis around the linearly unstable centre mode demonstrates that nonlinearity stabilises the flow at high polymer concentration while it destabilises the flow at low polymer concentration, indicating supercritical and subcritical bifurcations at high and low polymer concentrations, respectively (Wan *et al.* 2021). In contrast, the wall mode in the pipe flow remains linearly stable at all Re. However, using resolvent analysis, it has been found that the structure of the most strongly amplified mode by the linearised dynamics in viscoelastic pipe flow contains strong stress fluctuations localised at the critical layer (Zhang 2021), similar to the viscoelastic channel flow (Shekar *et al.* 2019), indicating a critical layer mechanism of the dynamics of EIT even in pipe flow. Further, there are common characteristics of the structures of EIT in both channel and pipe flows. For example, EIT in both channel and pipe flows exhibits near-wall vortical structures oriented in the direction perpendicular to the mean flow direction, and near-wall elongated streaks of streamwise velocity fluctuations aligned in the flow direction with a slight slope (Samanta *et al.* 2013; Lopez *et al.* 2019; Choueiri *et al.* 2021).

The basic characteristics of EIT in channel and pipe flows are fundamentally 2-D (Sid *et al.* 2018; Lopez *et al.* 2019). Therefore, in the present study, we investigate the dynamics of EIT in axisymmetric pipe flow. We perform direct numerical simulations of EIT using a spectral method. To analyse the dynamics, we introduce a viscoelastic variant of SPOD (Towne *et al.* 2018), which we refer to as 'VESPOD', that enables us to investigate the well-defined structures underlying EIT that evolve coherently in time. As detailed below, VESPOD is based on the total mechanical energy (kinetic plus elastic) of the flow, enabling an energy-based modal decomposition that contains both velocity and polymer stress fields. The eigenvalue spectrum of VESPOD exhibits distinct peaks, and by analysing those peaks, we find that the dynamics of EIT in pipe flow, in the parameter regime studied, is dominated by three distinct families of travelling waves. We also explore the effects of the domain length, Re and Wi on the dynamics of EIT and the travelling waves underlying its dynamics, and comment on the relation between EIT in pipe and channel flow. The remaining part of the paper has been organised as follows: § 2 discusses the methodology, § 3 focuses on results and discussion, and § 4 concludes with the findings of the study.

https://doi.org/10.1017/jfm.2026.11909 Published online by Cambridge University Press

2. Formulation and governing equations

2.1. *Direct numerical simulations of EIT*

The flow is governed by the conservation of momentum and mass, described by the equations

$$\frac{\partial \boldsymbol{u}}{\partial t} + \boldsymbol{u}\cdot\boldsymbol{\nabla}\boldsymbol{u} = -\boldsymbol{\nabla}p + \frac{\beta}{Re}\nabla^2\boldsymbol{u} + \frac{1-\beta}{Re}\boldsymbol{\nabla}\cdot\boldsymbol{\tau}_p + F(t)\,\boldsymbol{e}_z, \quad \boldsymbol{\nabla}\cdot\boldsymbol{u} = 0, \tag{2.1}$$

where $\boldsymbol{u}$ and p represent the non-dimensional velocity field and pressure field, respectively. The Reynolds number is defined as $Re = \rho U_c R/\eta$, where ρ and η are the density and zero shear rate viscosity of the fluid. The pipe radius (R) and the Newtonian laminar centreline velocity (U_c) are the characteristic length and velocity scales, respectively. The viscosity ratio β represents the contribution of solvent viscosity (η_s) to the zero shear solution viscosity, and is defined as $\beta = \eta_s/\eta$. The contribution of polymer chains to the stress tensor in the momentum equation is denoted as $\boldsymbol{\tau}_p$, and we use the FENE-P constitutive equation having polymer molecular diffusion to model it (Bird *et al.* 1987):

$$\frac{\partial \boldsymbol{\alpha}}{\partial t} + \boldsymbol{u}\cdot\boldsymbol{\nabla}\boldsymbol{\alpha} - \boldsymbol{\alpha}\cdot\boldsymbol{\nabla}\boldsymbol{u} - (\boldsymbol{\alpha}\cdot\boldsymbol{\nabla}\boldsymbol{u})^{\mathrm{T}} = -\boldsymbol{\tau}_p + \frac{1}{ReSc}\nabla^2\boldsymbol{\alpha}, \tag{2.2}$$

$$\boldsymbol{\tau}_p = \frac{1}{Wi}\left(\frac{\boldsymbol{\alpha}}{1-\mathrm{tr}(\boldsymbol{\alpha})/b} - \boldsymbol{I}\right), \tag{2.3}$$

where $\boldsymbol{\alpha}$, $\boldsymbol{I}$ and b are the conformation tensor, the identity tensor and the maximum extensibility of the polymer chain, respectively. The Weissenberg number is defined as $Wi = \lambda U_c/R$, where λ is the polymer relaxation time. We keep the molecular diffusion in the evolution equation of the conformation tensor (2.2) to ensure numerical stability. The strength of molecular diffusion is controlled by the Schmidt number $Sc = \eta/\rho D$, where D is the diffusion coefficient.

We perform numerical simulations for the axisymmetric pipe flow EIT. We consider no-slip boundary conditions on the wall of the pipe ($r = 1$), and axisymmetric boundary conditions at the centre of the pipe ($r = 0$). The finite molecular diffusion of the polymer chains requires boundary conditions for the governing equation of the conformation tensor (2.2). At the wall ($r = 1$), we solve (2.2) considering $1/Sc = 0$, and use the respective value of $\boldsymbol{\alpha}$ as the boundary condition. In the streamwise direction, we consider periodic boundary conditions. The volumetric flow through the pipe is kept constant at the Newtonian laminar value by tuning the body force ($F(t)$) at each time step.

We used Dedalus (Burns *et al.* 2020) to perform direct numerical simulations using the spectral method. The code validation can be found in Appendix A. We consider viscosity ratio $\beta = 0.97$ representing the extreme dilute limit, and $b = 6400$ corresponding to high-molecular-weight polymer chains (500 kDa polyacrylamide). The length of the computational domain is $L = 5 \times n$, where n is an integer. We used $N_z \times n = 256 \times n$ Fourier basis functions in the streamwise direction, and $N_r = 512$ Chebyshev basis functions in the radial direction. For time stepping, we use a second-order two-stage implicit–explicit Runge–Kutta scheme with fixed time step size $\Delta t = 0.001$ (unless stated otherwise). We consider molecular diffusion ($Sc = 250$) similar to previous studies (Sid *et al.* 2018; Kumar & Graham 2024). The simulations have been initiated with sufficiently large random perturbations in the state variables to trigger EIT. The simulation data corresponding to the initial 200 time units are dropped to make sure that the dynamics is fully developed. We also performed a sensitivity analysis of the EIT dynamics on Sc and mesh resolution (Appendix B), and continue with the parameters mentioned above as they capture the essential physics with affordable computational cost.

https://doi.org/10.1017/jfm.2026.11909 Published online by Cambridge University Press

2.2. *The VESPOD*

To analyse the EIT dataset for pipe flow, we use a viscoelastic variant of SPOD (VESPOD), which allows the modal decomposition of the velocity and polymeric stress fields together. We note that the flow displays translation symmetry in the streamwise (z) direction, in which case the Fourier basis functions are optimal in terms of energy (Holmes *et al.* 2012). To embed this symmetry in our VESPOD framework, first we Fourier-transform state variables in the streamwise direction, and then perform VESPOD decomposition wavenumber-by-wavenumber. The VESPOD represents the frequency-by-frequency VEPOD decomposition of a Fourier-transformed (in the temporal direction) time-dependent dataset (Holmes *et al.* 2012; Wang *et al.* 2014), where VEPOD is a viscoelastic variant of POD (Kumar *et al.* 2025). Hence VESPOD seeks to find the basis function $\boldsymbol{\psi}(\kappa, r, f)$ that maximises the objective function

$$E\left\{|\langle \boldsymbol{q}(\kappa, r, f), \boldsymbol{\psi}(\kappa, r, f)\rangle|^2\right\}, \tag{2.4}$$

given the constraint $\langle \boldsymbol{\psi}(\kappa, r, f), \boldsymbol{\psi}(\kappa, r, f)\rangle = 1$, where $E\{\cdot\}$ and $|\cdot|$ represent expectation and modulus operations on the data ensemble, respectively. The quantity $\boldsymbol{q}(\kappa, r, f)$ represents a vector containing state variables having scaled streamwise wavenumber κ (defined as the number of wavelengths per domain length) and temporal oscillation frequency f. In VESPOD, $\boldsymbol{q}$ is defined as

$$\boldsymbol{q} = \left[\boldsymbol{u}', \boldsymbol{T}'\right], \tag{2.5}$$

where the stretch tensor is $\boldsymbol{T} = \sqrt{(1-\beta)/(ReWi)}\,\boldsymbol{\theta}$, and $\boldsymbol{\theta}\cdot\boldsymbol{\theta} = \boldsymbol{\alpha}/(1-\mathrm{tr}(\boldsymbol{\alpha})/b)$ (Wang *et al.* 2014). The superscript prime ($'$) represents the perturbation from the mean (averaged over t and z). The inner product $\langle\cdot,\cdot\rangle$ in the objective function (2.4) has been defined as

$$\langle \boldsymbol{q}, \boldsymbol{\psi}\rangle = 2\pi \int_0^1 \boldsymbol{q}(r)\cdot\boldsymbol{\psi}(r)\, r\,\mathrm{d}r. \tag{2.6}$$

The specific definition of variable $\boldsymbol{q}$ leads to the following inner product of $\boldsymbol{q}$ with itself:

$$\langle \boldsymbol{q}, \boldsymbol{q}\rangle = 2\pi \int_0^1 \left\{\boldsymbol{u}'\cdot\boldsymbol{u}' + \frac{1-\beta}{ReWi}\boldsymbol{\theta}' : \boldsymbol{\theta}'\right\} r\,\mathrm{d}r. \tag{2.7}$$

This inner product and choice of $\boldsymbol{q}$ are chosen because in the limit $b\to\infty$, (2.7) becomes the total mechanical energy of the flow and is thus a natural and interpretable inner product for analysis of viscoelastic flows. In this limit, VESPOD yields an optimal decomposition in terms of total mechanical energy. For b finite, the identification with total mechanical energy is approximate but is nevertheless useful. We also plot the probability distribution function (PDF) of $\mathrm{tr}(\boldsymbol{\alpha})/b$ to find the distribution of stretching of polymeric chains in EIT (Appendix C). The probability of a large value of $\mathrm{tr}(\boldsymbol{\alpha})/b$ is small, indicating that the inner product used in the present study provides a good representative of the total mechanical energy.

The maximisation of the objective function (2.4) leads to the self-adjoint eigenvalue problem

$$2\pi \int_0^1 E\{\boldsymbol{q}(\kappa, r, f)\,\boldsymbol{q}^*(\kappa, \rho, f)\}\,\boldsymbol{\psi}(\kappa, \rho, f)\,\rho\,\mathrm{d}\rho = \sigma\boldsymbol{\psi}(\kappa, r, f), \tag{2.8}$$

which gives an infinite set of eigenmodes $\{\sigma_j, \boldsymbol{\psi}_j(\kappa, r, f)\}$, which are arranged in decreasing value of (approximate) mechanical energy. The state variables can be

https://doi.org/10.1017/jfm.2026.11909 Published online by Cambridge University Press

reconstructed using VESPOD modes as

$$\tilde{\boldsymbol{q}}(\kappa, r, f) = \sum_{j=1}^{\infty} a_j(\kappa, f)\, \boldsymbol{\psi}_j(\kappa, r, f), \tag{2.9}$$

where $a_j(\kappa, f) = \langle \boldsymbol{q}(\kappa, r, f), \boldsymbol{\psi}_j(\kappa, r, f) \rangle$.

To obtain the VESPOD of a discrete time series, the data matrix containing the Fourier coefficients of the structures having wavenumber κ of the discrete time series of snapshots N_t is constructed as

$$\boldsymbol{Q}_\kappa = [\boldsymbol{q}_{1,\kappa}, \boldsymbol{q}_{2,\kappa}, \ldots, \boldsymbol{q}_{N_t,\kappa}], \tag{2.10}$$

where $\boldsymbol{q}_{i,\kappa} = \boldsymbol{q}(\kappa, r, t_i)$. The computation of VESPOD using (2.8) requires an ensemble of independent realisations. In practice, when only a single time-resolved data point is available, but the flow is chaotic (adequate temporally decorrelated), the ensemble can be constructed by using data from different time windows of a very long time series (Welch 1967). Therefore, multiple realisations of the flow time series have been generated by dividing the data matrix into overlapping blocks as

$$\boldsymbol{Q}^n_\kappa = [\boldsymbol{q}^n_{1,\kappa}, \boldsymbol{q}^n_{2,\kappa}, \ldots, \boldsymbol{q}^n_{m,\kappa}, \ldots, \boldsymbol{q}^n_{N_f,\kappa}], \quad n = 1, 2, \ldots, N_b, \tag{2.11}$$

where N_b and N_f are the number of blocks and the number of snapshots in each block. For N_o overlapping snapshots in each block, the entries of the data matrices $\boldsymbol{Q}^n_\kappa$ and $\boldsymbol{Q}_\kappa$ are related as $\boldsymbol{q}^n_{m,\kappa} = \boldsymbol{q}_{m+(n-1)(N_f-N_o),\kappa}$. Next, we compute the discrete Fourier transform (DFT) of each block in the temporal direction. To minimise the spectral leakage resulting from the non-periodicity of the data in each block during the estimation of the DFT, we compute the DFT of the windowed data:

$$\boldsymbol{Q}^{n,w}_\kappa = [w_1 \boldsymbol{q}^n_{1,\kappa}, w_2 \boldsymbol{q}^n_{2,\kappa}, \ldots, w_m \boldsymbol{q}^n_{m,\kappa}, \ldots, w_{N_f} \boldsymbol{q}^n_{N_f,\kappa}], \tag{2.12}$$

where w_m represents the nodal value of the symmetric Hamming window function and is given as

$$w_m = 0.54 - 0.46 \cos\left(\frac{2\pi(m-1)}{N_f - 1}\right). \tag{2.13}$$

The Fourier coefficients of the temporal DFT of $\boldsymbol{Q}^{n,w}_\kappa$ are given as

$$\tilde{\boldsymbol{Q}}^n_\kappa = [\tilde{\boldsymbol{q}}^n_{1,\kappa}, \tilde{\boldsymbol{q}}^n_{2,\kappa}, \ldots, \tilde{\boldsymbol{q}}^n_{m,\kappa}, \ldots, \tilde{\boldsymbol{q}}^n_{N_f,\kappa}], \tag{2.14}$$

where $\tilde{\boldsymbol{q}}^n_{m,\kappa}$ represents the Fourier coefficient of wavenumber κ at frequency f_m in the nth block. Now the Fourier coefficients at frequency f_m are collected from each block, and a new data matrix $\tilde{\boldsymbol{Q}}_{m,\kappa}$ is constructed as

$$\tilde{\boldsymbol{Q}}_{m,\kappa} = [\tilde{\boldsymbol{q}}^1_{m,\kappa}, \tilde{\boldsymbol{q}}^2_{m,\kappa}, \ldots, \tilde{\boldsymbol{q}}^n_{m,\kappa}, \ldots, \tilde{\boldsymbol{q}}^{N_b}_{m,\kappa}]. \tag{2.15}$$

The VESPOD modes at frequency f_m can be obtained by calculating the eigenmodes of the discretised cross-spectral density matrix $\boldsymbol{S}_{m\kappa} = \tilde{\boldsymbol{Q}}_{m,\kappa}\tilde{\boldsymbol{Q}}^*_{m,\kappa}$ by solving the eigenvalue problem

$$\boldsymbol{S}_{m,\kappa}\boldsymbol{W}\boldsymbol{\psi}_{m,\kappa} = \boldsymbol{\psi}_{m,\kappa}\boldsymbol{\sigma}_{m,\kappa}, \tag{2.16}$$

where $\boldsymbol{\psi}_{m,\kappa} = \boldsymbol{\psi}(\kappa, r, f_m)$ represents the VESPOD mode structures at wavenumber κ and frequency f_m, and diagonal matrix $\boldsymbol{\sigma}_{m,\kappa}$ represents mechanical energy associated with respective mode structures. The matrix $\boldsymbol{W}$ is a positive-definite weighting matrix, which properly accounts for the integration on a non-uniform discrete grid.

https://doi.org/10.1017/jfm.2026.11909 Published online by Cambridge University Press

The eigenmode computation of (2.16) is expensive. To overcome this challenge, the following eigenvalue problem is solved:

$$\tilde{\boldsymbol{Q}}^{*}_{m,\kappa}\boldsymbol{W}\tilde{\boldsymbol{Q}}_{m,\kappa}\boldsymbol{\Theta}_{m,\kappa}=\boldsymbol{\Theta}_{m,\kappa}\boldsymbol{\sigma}_{m,\kappa}. \tag{2.17}$$

This is faster to compute because the number of flow realisations (N_b) is much smaller than the number of grid points. This analogous problem gives the same non-zero eigenvalues as (2.16), and their eigenvectors are related as

$$\boldsymbol{\psi}_{m,\kappa}=\tilde{\boldsymbol{Q}}_{m,\kappa}\boldsymbol{\Theta}_{m,\kappa}\boldsymbol{\sigma}^{-1/2}_{m,\kappa}. \tag{2.18}$$

The VESPOD mode structures having wavenumber κ and frequency f_m can be projected in the physical space as

$$\boldsymbol{\psi}_{m}(z,r)=\boldsymbol{\psi}_{m,\kappa}\,\mathrm{e}^{\mathrm{i}2\pi\kappa z/L}. \tag{2.19}$$

We modify the MATLAB tool originally developed by Schmidt (2022) to perform VESPOD analysis of EIT in pipe flow. We used data corresponding to 600 time units sampled at time interval $\Delta t_s=0.025$ time units, leading to a total of 24 000 snapshots. The multiple realisations of the flow for most of the cases have been constructed by dividing the data into blocks having $N_f=2000$ snapshots in each block with 50 % overlap. This leads to a total of 23 blocks, which is sufficient for a converged computation of VESPOD. The current choices of Δt_s and N_f lead to frequency resolution $\Delta f=1/(\Delta t_s\,N_f)=0.02$. However, for $\kappa=1$ structures, we have used $\Delta f=0.01$ by considering $N_f=4000$ to properly resolve distinct peaks in the eigenvalue spectra. A coarse frequency resolution may fail to resolve distinct spectral peaks, whereas an excessively fine frequency resolution can reduce statistical convergence and can generate numerous closely spaced peaks by resolving weak temporal variability within broadband structures, thereby making it difficult to isolate the dominant energetic structures. Therefore, an optimal value of Δf is chosen to balance frequency resolution and statistical convergence (Appendix D).

3. Results and discussion

We use VESPOD analysis to uncover the structures underlying the dynamics of EIT in axisymmetric pipe flow at several parameter regimes and domain lengths. First, we analyse dynamics at $Re=3000$, $Wi=35$ and $L=5$ (§ 3.1). Then we discuss dynamics of EIT in a longer domain ($L=10$) (§ 3.2) and the effect of Re and Wi on EIT (§ 3.3). Finally, we discuss the relationship between EIT in the pipe and channel flows, and their link to linear dynamics (§ 3.4).

3.1. *The EIT at $Re=3000$, $Wi=35$ and $L=5$*

Figure 1 depicts instantaneous snapshots of state variables and their temporal means for the dynamics of EIT at $Re=3000$, $Wi=35$ and $L=5$. The dynamics of EIT has well-defined means (figures 1*d,e*). Therefore, we report the perturbations of different state variables from their temporal means. The dynamics consists of weak velocity fluctuations, consistent with the nature of EIT (figures 1*a,b*). The radial velocity field (u'_r) has distinct large-scale dynamic patterns dominating the region between the pipe centreline and the wall (figure 1(*a*), supplementary movie 1 are available at https://doi.org/10.1017/jfm.2026.11909). The streamwise velocity fluctuation (u'_z) has thin elongated streaks close to the wall; however, it contains large-scale structures in the vicinity of the pipe centreline (figure 1(*b*), supplementary movie 2). The polymeric stress field contains the formation of thin sheets of high polymeric stress in most of the pipe,

https://doi.org/10.1017/jfm.2026.11909 Published online by Cambridge University Press

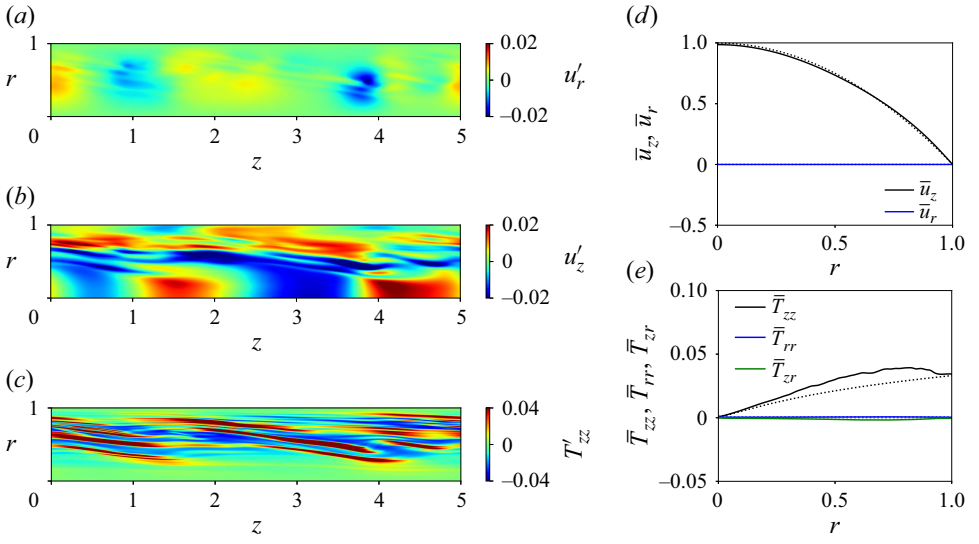


Figure 1. Instantaneous (a) radial velocity, (b) streamwise velocity, and (c) zz-component of the stretch tensor of EIT in axisymmetric pipe flow at $Re = 3000$, $Wi = 35$ and $L = 5$. Means (averaged over z and t) of (d) velocity components and (e) stretch components. Dotted lines in (d,e) represent the laminar profiles at the same parameter.

with slight clustering near the pipe wall (Appendix B, supplementary movie 3). In the present paper, we use the scaled stretch field ($\boldsymbol{T}$) to represent the polymeric stress field (figure 1c), and due to the appropriate scaling of the stretch field, which is based on its contribution to the mechanical energy, the velocity and stretch fields have similar magnitude (figures 1a–c). This observation provides quantitative evidence that for EIT, both inertia and elasticity are equally important. The zz-component of the polymeric stress (and stretch) tensor dominates the stress field. Therefore, we report only T'_{zz} in the present study. The stretch field (T'_{zz}) contains thin inclined sheets of high stretch fluctuations situated well away from the pipe centre $r = 0$ (figure 1c).

The VESPOD energy spectrum of the structures having wavenumber $\kappa = 1$ has been depicted in figure 2(a). The leading eigenvalue (integrated over all frequencies) contributes approximately 78 % to the total variance (approximate mechanical energy), and there are three distinct peaks in the leading eigenvalue, suggesting that the mode structures corresponding to these peaks have a large contribution to the overall dynamics. In figure 3, we visualise the mode structures corresponding to different peaks in the energy spectrum. The radial velocity component has large-scale structures located away from the pipe centreline, which move from the location close to the pipe wall for the peak at low frequency to the vicinity of the pipe centreline for the peak at high frequency (figures 3a–c). The streamwise velocity component has large-scale structures centred at the pipe centreline, which shrink in the radial direction as the frequency of the peak increases; however, it has elongated patches of velocity fluctuations close to the wall (figures 3d–f). The stretch field contains a layer having thin inclined sheets of high stretch fluctuations, and the location of this layer moves to the centreline of the pipe as the frequency increases (figures 3g–i). These three structures are distinct travelling waves; their wave speeds $c_w = fL/\kappa$ can be given as $c_{w,1}$, $c_{w,2}$ and $c_{w,3}$ in ascending order of their wave speed, and corresponding peaks in the energy spectrum as peak index 1, 2 and 3, respectively.

The concept of critical layer has proven useful in the understanding of transitional flows, as for travelling fluctuations it provides the most favourable place to exchange energy

https://doi.org/10.1017/jfm.2026.11909 Published online by Cambridge University Press

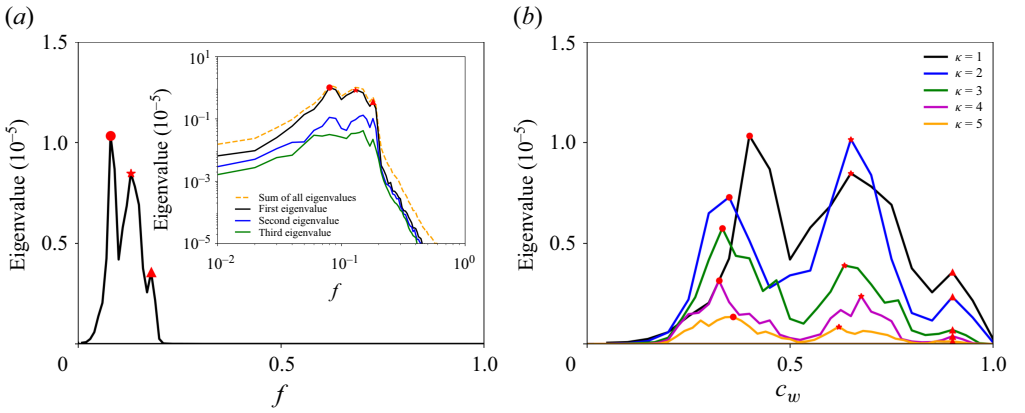


Figure 2. (*a*) Leading eigenvalue of the VESPOD energy spectrum of the structures having wavenumber $\kappa = 1$ underlying EIT at $Re = 3000$, $Wi = 35$ and $L = 5$; inset shows spectrum in log–log scale. (*b*) Leading eigenvalues of the VESPOD energy spectra for structures having different wavenumbers. Red symbols represent the peaks in the leading eigenvalues (circle, star and triangle are first, second and third peaks, respectively).

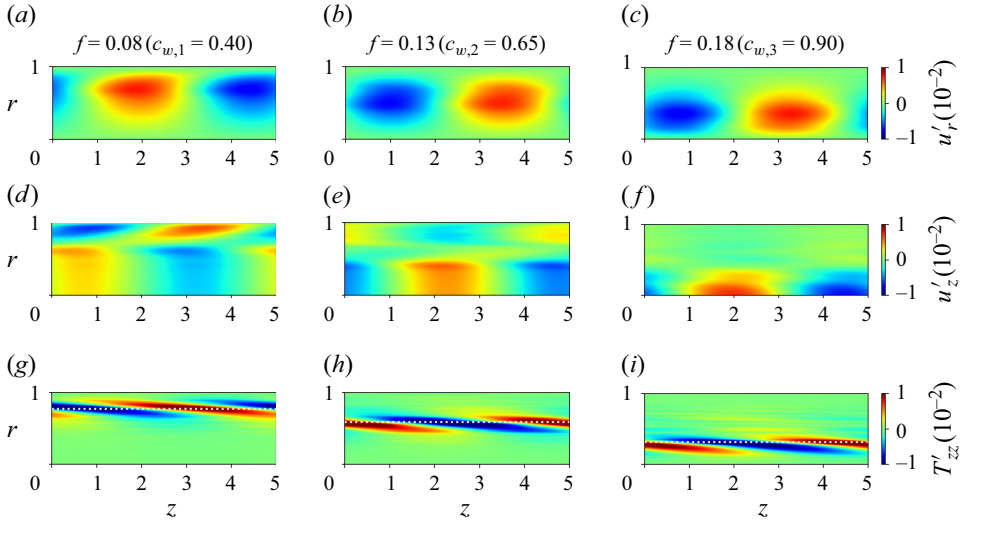


Figure 3. The VESPOD mode structures of (*a*–*c*) radial velocity (u_r'), (*d*–*f*) streamwise velocity (u_z'), and (*g*–*i*) the zz-component of the stretch tensor (T_{zz}') corresponding to the peaks in the leading eigenvalue of the VESPOD energy spectrum of $\kappa = 1$. Locations of critical layers have been denoted with white dotted lines in (*g*–*i*). Other parameters are $Re = 3000$, $Wi = 35$ and $L = 5$.

between the base flow and fluctuations (Drazin & Reid 1981). Therefore, we also explore the relationship between the critical layer of the travelling wave and the mode structures. As the mean velocity profile is close to the laminar parabolic profile (figure 1*d*), the location of the critical layer can be given as $r_c = \sqrt{1 - c_w}$. The sheets of high polymeric stretch fluctuations in the VESPOD modes are localised around the location of the critical layer (figures 3*g*–*i*). This observation is consistent with the structures of travelling waves underlying EIT in channel flow (Shekar *et al.* 2019; Kumar & Graham 2024).

To explore the mechanism of the emergence of sheets in the polymeric stress field, in figure 4 we plot the streamlines of velocity fields that are constructed from the mean flow

https://doi.org/10.1017/jfm.2026.11909 Published online by Cambridge University Press

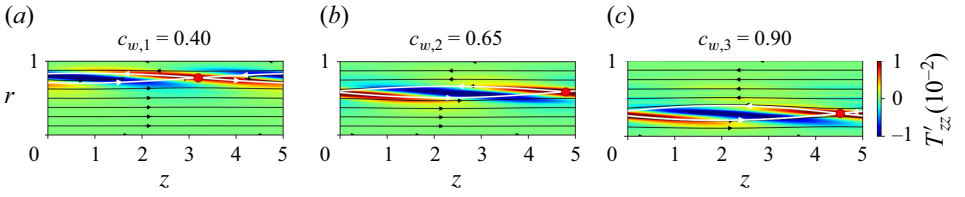


Figure 4. Streamlines of a velocity field consisting of the mean flow and a small component of the peak VESPOD mode at (*a*) $f = 0.08$ ($c_{w,1} = 0.40$), (*b*) $f = 0.13$ ($c_{w,2} = 0.65$) and (*c*) $f = 0.18$ ($c_{w,3} = 0.90$) from figure 2(*a*) are shown in reference frames moving with their respective wave speeds, and are superimposed on the zz-component of the stretch tensor (T'_{zz}). The red circles denote hyperbolic stagnation points, and the streamlines passing through them are shown in white.

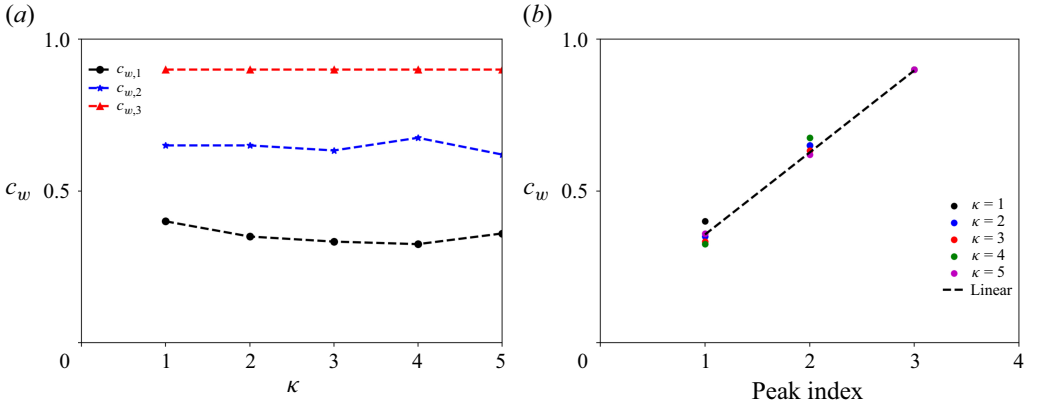


Figure 5. Wave speeds of the VESPOD mode structures corresponding to the peaks in the energy spectra: (*a*) wave speed versus wavenumber, and (*b*) wave speed versus peak index. Parameter values are $Re = 3000$, $Wi = 35$ and $L = 5$.

plus a small contribution from the peak VESPOD mode at the peaks in figure 2(*a*), in the reference frame moving with their respective wave speeds, along with T'_{zz}. There is a hyperbolic stagnation point in the velocity field (in the reference frame moving with the wave speed) at the critical layer of the travelling wave, where the flow is extension dominated. Polymeric chains get highly stretched as they approach and depart such a stagnation point, leading to the formation of thin polymeric sheets at the critical layer. This critical layer mechanism is consistent with the critical layer mechanism of the origin of polymeric sheets in channel flow EIT (Shekar *et al.* 2019).

The VESPOD energy spectra of higher wavenumber structures have characteristics similar to those at $\kappa = 1$. The leading eigenvalues contain most of the energy across the spectra of different wavenumber structures, and have three distinct peaks. In figure 2(*b*), we visualise the leading eigenvalues of VESPOD corresponding to different κ as a function of wave speed. For a given peak index, the wave speeds of the mode structures are nearly independent of wavenumber, implying that the higher wavenumber structures ($\kappa \geqslant 2$) are simple harmonics of the fundamental wavenumber structure ($\kappa = 1$). This is also evident from figure 5. The travelling waves corresponding to each peak index belong to the respective unique family of travelling waves having unique wave speed (figure 5*a*), and the wave speed of the family of travelling waves increases almost linearly with the peak index (figure 5*b*).

https://doi.org/10.1017/jfm.2026.11909 Published online by Cambridge University Press

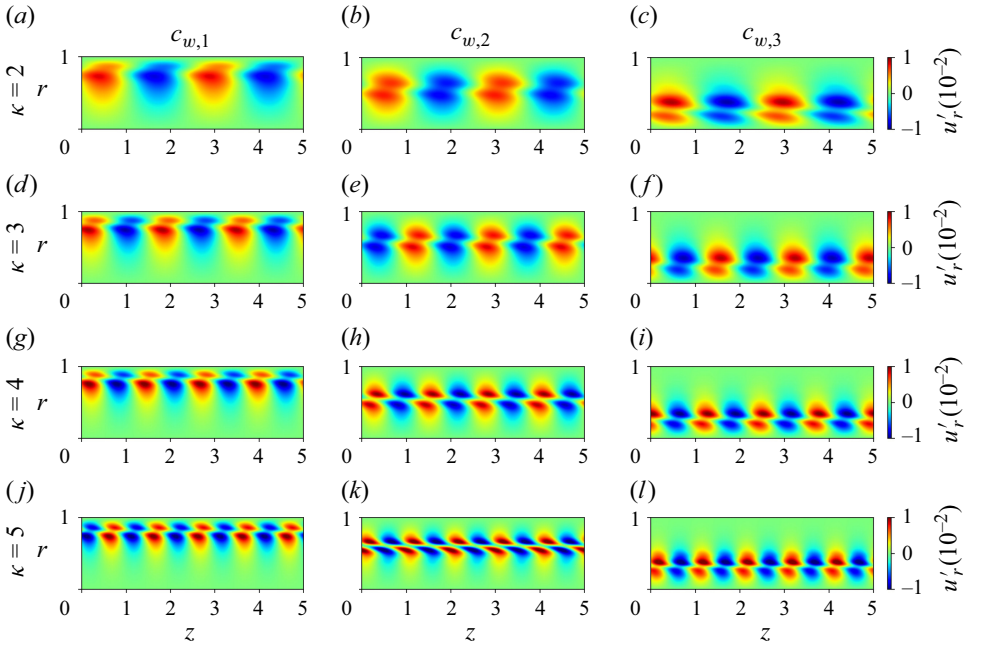


Figure 6. The VESPOD mode structures of u_r' corresponding to different peaks in the leading eigenvalue of energy spectrum of wavenumbers $(a-c)$ $\kappa = 2$, $(d-f)$ $\kappa = 3$, $(g-i)$ $\kappa = 4$, and $(j-l)$ $\kappa = 5$. Other parameters are $Re = 3000$, $Wi = 35$ and $L = 5$.

In addition, we depict u_r' and T_{zz}' of mode structures corresponding to the three distinct peaks in the VESPOD energy spectra of higher wavenumber structures ($\kappa \geqslant 2$) in figures 6 and 7, respectively. The radial velocity component has large-scale structures, and these structures have a partition line oriented in the streamwise direction that divides the structures into two parts (figure 6). For each wavenumber, the location of the partition line moves to the centreline of the pipe as the wave speed increases. However, for a given wave speed (i.e. peak index), the location of the partition line is insensitive to the wavenumber. The stretch field is characterised by the formation of a layer, again localised at the critical layer position, having thin inclined sheets of high stretch fluctuations (figure 7). For a given wave speed, the locations of this layer for different wavenumber structures coincide with each other. However, they move to the pipe centreline as the wave speed increases for each wavenumber structure. Further, the location of the partition line of the structure in radial velocity coincides with the critical layer, and hence the polymeric sheets.

The discussion so far demonstrates that the dynamics of EIT in pipe flow at $Re = 3000$, $Wi = 35$ and $L = 5$ is dominated by three distinct families of travelling waves, where higher wavenumber structures ($\kappa \geqslant 2$) are the simple harmonics of the respective fundamental waves ($\kappa = 1$). There also exist some relationships among different families of travelling waves. For example, the sheets of high polymeric stretch fluctuations of $c_{w,1}$ are located in the vicinity of the wall of the pipe, and the polymeric stretch sheets of $c_{w,2}$ are confined in the region bounded by the pipe centreline and polymeric stretch sheets of $c_{w,1}$. Similarly, the sheets of $c_{w,3}$ are bounded by the pipe centreline and the sheets of $c_{w,2}$. Thus the polymeric sheets of different families of travelling waves exhibit a nested arrangement, where the polymeric sheets of faster waves are confined by the polymeric sheets of immediately slower waves. A similar nesting relationship among the dominant

https://doi.org/10.1017/jfm.2026.11909 Published online by Cambridge University Press

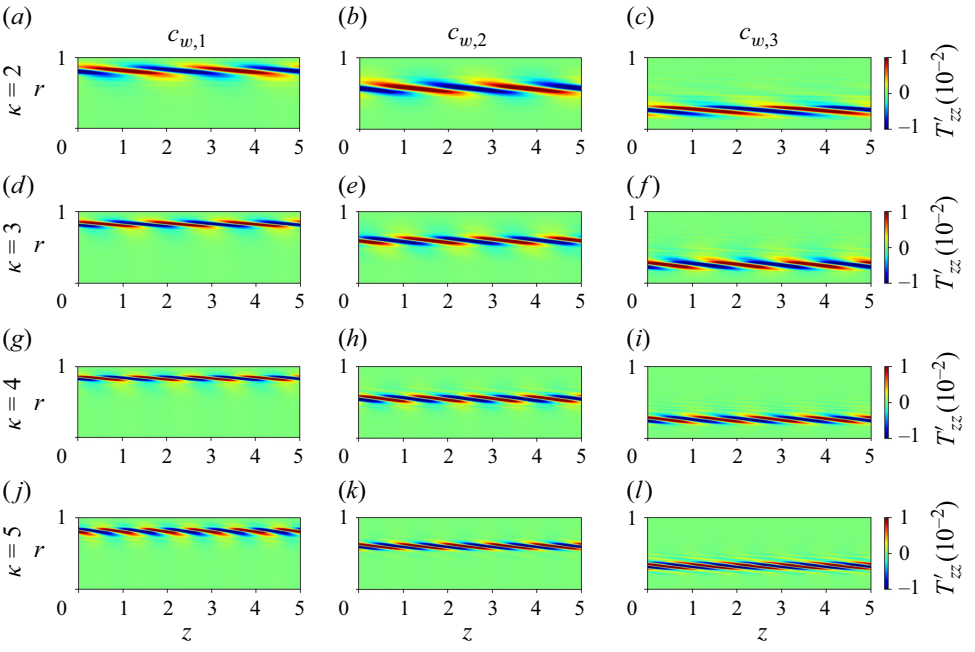


Figure 7. The VESPOD mode structures of T'_{zz} corresponding to different peaks in the leading eigenvalue of energy spectrum of wavenumbers $(a-c)\ \kappa = 2$, $(d-f)\ \kappa = 3$, $(g-i)\ \kappa = 4$, and $(j-l)\ \kappa = 5$. Other parameters are $Re = 3000$, $Wi = 35$ and $L = 5$. These structures correspond to the velocity structures shown in figure 6.

travelling waves underlying EIT in channel flow has been observed (Kumar & Graham 2024).

3.2. *The EIT at* $Re = 3000$, $Wi = 35$ *and* $L = 10$

To explore the effects of pipe length on EIT dynamics, we performed a simulation in a domain twice the length of the pipe discussed in § 3.1, but at the same *Re* and *Wi*. The velocity and stretch fields corresponding to EIT in the longer pipe are shown in figure 8. We analyse VESPOD spectra to identify the dominant coherent structures underlying them, and how pipe length affects them. The leading eigenvalue of the VESPOD spectrum of each wavenumber structure contains a dominant contribution to the total mechanical energy and has three distinct peaks, similar to the shorter pipe. We visualise the leading eigenvalue of different wavenumber structures as a function of wave speed, and find that the wave speeds corresponding to peaks in the leading eigenvalues are nearly independent of the wavenumber of structures (figure 9*a*). This shows that travelling waves with high wavenumber ($\kappa \geqslant 2$) are harmonics of the fundamental wave ($\kappa = 1$). This is also evident from figure 9(*b*), where we see three distinct families of travelling waves originating from the simple harmonic excitation of respective fundamental waves. We have also visualised the structures of different travelling waves in figure 10. We emphasise that the travelling waves having an even wavenumber ($\kappa = 2, 4, \ldots$) in the pipe with $L = 10$ are the same travelling waves discovered in the pipe with $L = 5$. However, the travelling waves with an odd wavenumber ($\kappa = 1, 3, 5, \ldots$) in the pipe with $L = 10$ are new and do not exist in the pipe with $L = 5$ because they do not satisfy the periodicity in the shorter domain. We also note that the energy associated with $\kappa = 2$ structures is higher than that of $\kappa = 1$ structures (at least for the first two families of travelling waves), suggesting that the structures having

https://doi.org/10.1017/jfm.2026.11909 Published online by Cambridge University Press

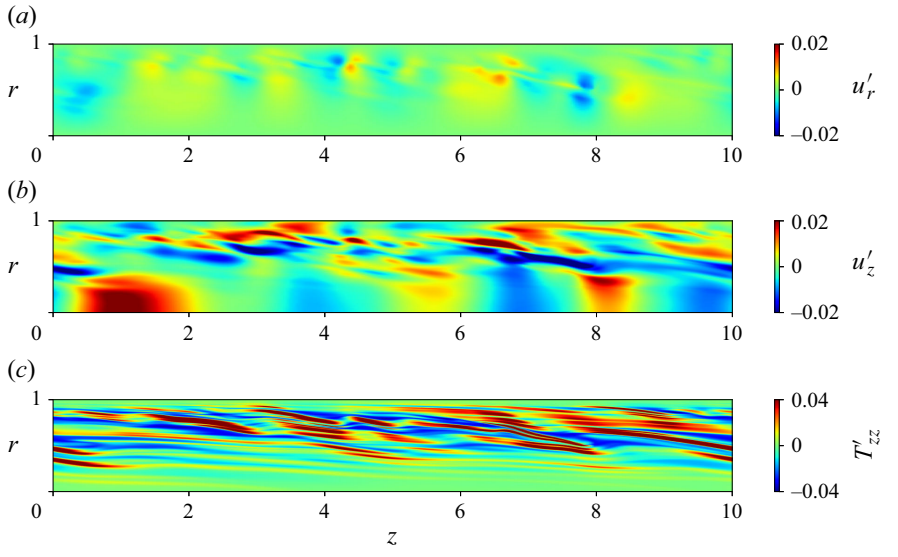


Figure 8. Snapshots of (*a*) radial velocity, (*b*) streamwise velocity, and (*c*) the zz-component of the stretch tensor of EIT in axisymmetric pipe flow at $Re = 3000$, $Wi = 35$ and $L = 10$.

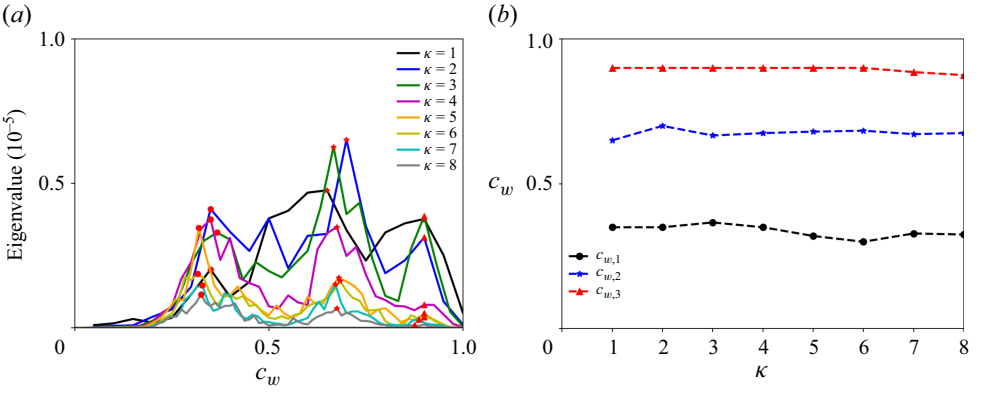


Figure 9. (*a*) Leading eigenvalues of the VESPOD energy spectra of different wavenumber structures at $Re = 3000$, $Wi = 35$ and $L = 10$. (*b*) Wave speeds of the travelling waves corresponding to the peaks in the leading eigenvalues of VESPOD energy spectra.

wavelength 5 units still dominate even in the pipe with $L = 10$ (figure 9*a*). This indicates that the pipe with $L = 5$ is long enough to capture the dominant structures.

3.3. *Effects of Re and Wi*

To explore the effects of Wi and Re on the dynamics of EIT, we analyse EIT at $Re = 3000$, $Wi = 70$, $L = 5$ (figures 11*a*–*c*) and $Re = 6000$, $Wi = 35$, $L = 5$ (figures 11*d*–*f*). The VESPOD energy spectrum at $Re = 3000$, $Wi = 70$ (figure 12*a*) exhibits characteristics similar to those of the spectrum at $Re = 3000$, $Wi = 35$ (figure 2*b*). The three distinct harmonic families of travelling waves persist even at $Wi = 70$, which is evident from the three distinct peaks in the leading eigenvalues of the energy spectra of different wavenumber structures. For EIT at $Wi = 70$, the speeds of these three families of travelling waves are the same as for the waves at $Wi = 35$, suggesting that Wi does not affect the

https://doi.org/10.1017/jfm.2026.11909 Published online by Cambridge University Press

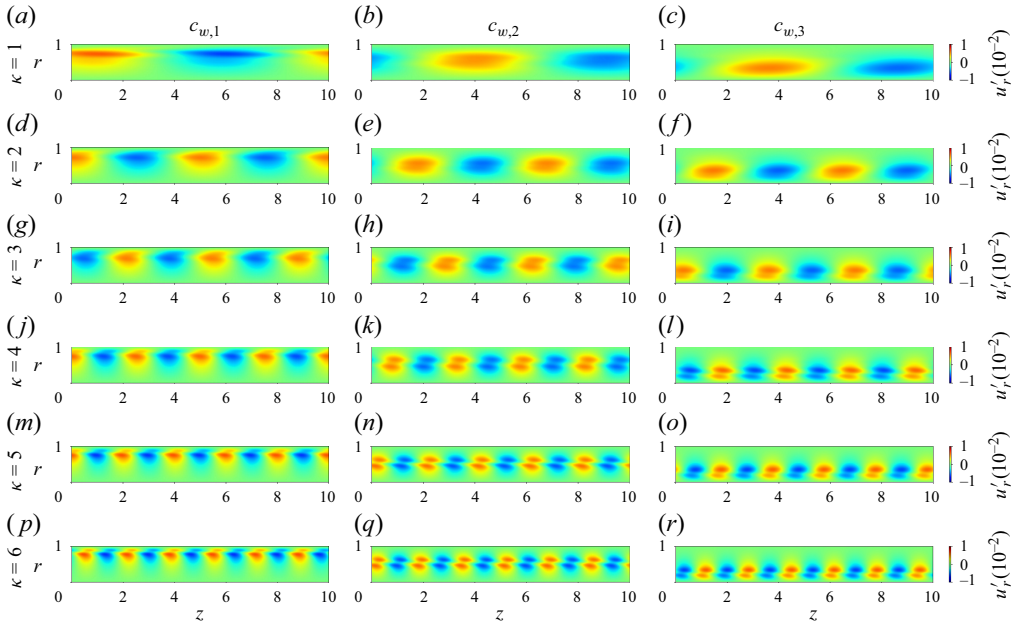


Figure 10. The VESPOD mode structures of u_r' corresponding to different peaks in the leading eigenvalue of the energy spectrum of different wavenumber structures in the pipe of length $L = 10$ ($Re = 3000$ and $Wi = 35$).

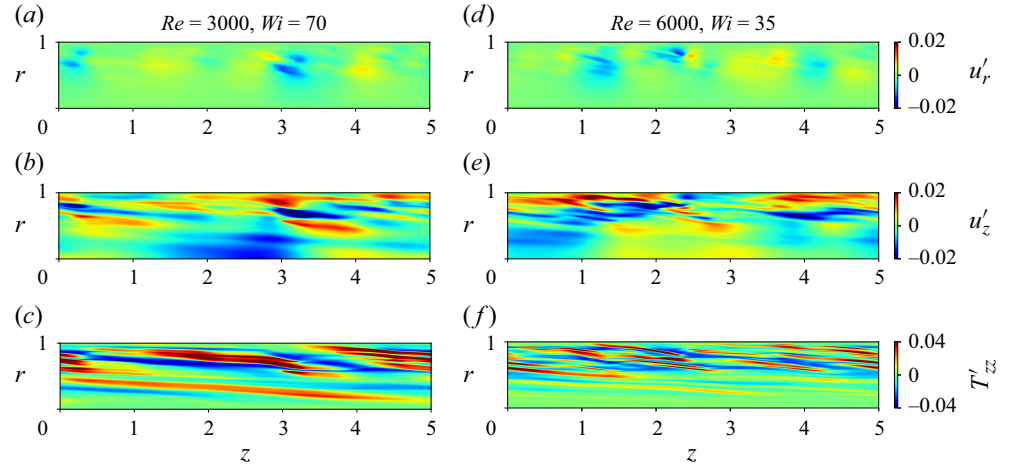


Figure 11. Snapshots of (a, d) radial velocity, (b, e) streamwise velocity, and (c, f) the zz-component of the stretch tensor of EIT in axisymmetric pipe flow at $(a-c)$ $Re = 3000$, $Wi = 70$ and $(d-f)$ $Re = 6000$, $Wi = 35$.

speeds of different travelling waves at a fixed Re. At higher value of Wi, along with three harmonic peaks in the leading eigenvalues of VESPOD energy spectra, we also observe additional distinct peaks for some wavenumber structures (figure 12(*a*), purple diamond symbol). These are non-harmonic modes, having energy comparable to the harmonic modes. The mode structures corresponding to the peaks at $Wi = 70$ are similar to those for $Wi = 35$. Therefore, here we only include the structures corresponding to the first three peaks in the leading eigenvalue of $\kappa = 1$ at $Re = 3000$ and $Wi = 70$ (figure 13). The mode

https://doi.org/10.1017/jfm.2026.11909 Published online by Cambridge University Press

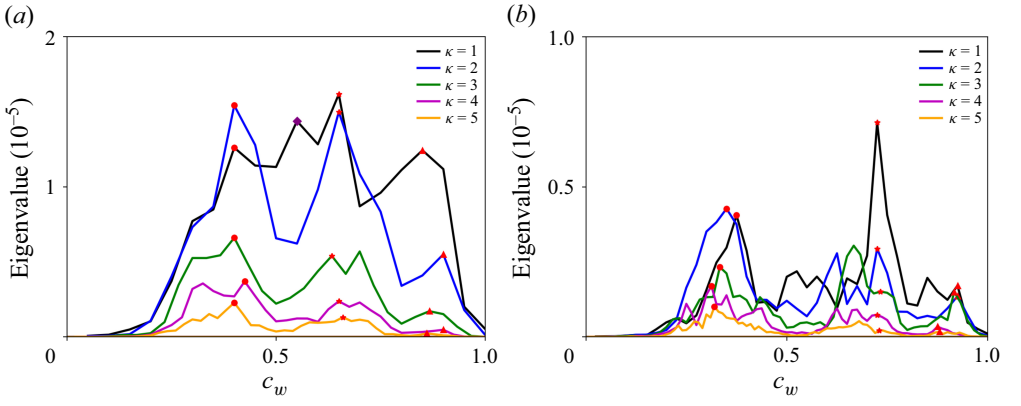


Figure 12. Leading eigenvalues of VESPOD energy spectra for different wavenumber structures at (*a*) $Re = 3000$, $Wi = 70$ and (*b*) $Re = 6000$, $Wi = 35$. Red symbols represent harmonic peaks, while a purple diamond symbol represents a non-harmonic peak.

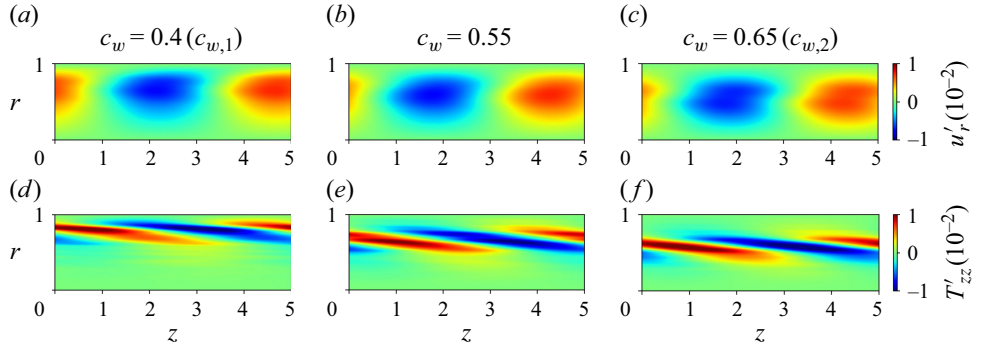


Figure 13. The VESPOD mode structures of (*a*–*c*) u_r' and (*d*–*f*) T_{zz}' corresponding to the first three peaks in the leading eigenvalue of $\kappa = 1$ at $Re = 3000$ and $Wi = 70$ (figure 12*a*). Here, (*b*,*e*) correspond to the structures of the non-harmonic peak (purple diamond in figure 12*a*); however, (*a*,*d*) and (*c*,*f*) represent harmonic peaks.

structures shown in figures 13(*a*, *d*) and 13(*c*, *f*) correspond to the fundamental wave of the first ($c_{w,1}$) and second ($c_{w,2}$) families of harmonic travelling waves. However, the structures in figures 13(*b*, *e*) correspond to the non-harmonic peak in the leading eigenvalue of the $\kappa = 1$ structure at $Re = 3000$ and $Wi = 70$ (figure 12*a*). We do not see any fundamental difference between the mode structures of the harmonic and non-harmonic peaks.

Further, we analyse dynamics at higher Re ($Re = 6000$), while keeping $Wi = 35$, the same as in § 3.1 (figure 12*b*). Again, there exist three dominant families of harmonic travelling waves. However, the speeds of the travelling waves at $Re = 6000$ are slightly different from those at $Re = 3000$. For example, the speed of the second family of travelling waves ($c_{w,2}$) at $Re = 6000$ is higher than that at $Re = 3000$. At larger Re, non-harmonic modes become increasingly important. As Wi or Re increases, the EIT dynamics becomes increasingly broadband and temporally complex, resulting in less distinct spectral peaks and weaker coherent travelling wave signatures. Accordingly, additional peaks emerge alongside the harmonic peaks at higher Re and Wi, indicating increasingly irregular nonlinear dynamics.

https://doi.org/10.1017/jfm.2026.11909 Published online by Cambridge University Press

3.4. *Relation to channel flow EIT and linear dynamics*

The dynamics of EIT in channel and pipe flows share several similarities, but also exhibit important differences. Even though both dynamics have similar first glance features such as the large-scale structures in wall-normal velocity and the formation of thin inclined sheets of high stress in the polymeric stress field, the dominant coherent structures underlying them are distinct. The EIT in channel flow is dominated by a family of non-harmonic travelling waves, whereas in pipe flow it is dominated by the three distinct families of harmonic travelling waves. The wall-normal velocity component of these travelling waves exhibits large-scale structures centred at the centreline in channel flow, whereas they are located away from the centreline in pipe flow. The streamwise velocity component of these waves exhibits regular structures in the vicinity of the centreline in pipe flow, whereas in channel flow, such distinct structures are located away from the centreline. However, the polymeric stress field in both channel and pipe flows contains sheets of high stress fluctuations at the critical layers of the travelling waves. Further, the polymeric sheets of faster travelling waves in both channel and pipe flows are confined by the polymeric sheets of their immediately slower travelling waves, leading to a nested arrangement of polymeric sheets in both dynamics.

The resolvent analysis, which is based on the response of linearised governing equations to an external forcing, provides the modes that optimally describe the linear growth. It has been demonstrated that the SPOD modes are the same as the resolvent modes for uncorrelated resolvent-mode expansion coefficients, which is the case for the white-noise forcing of linear dynamics (Towne *et al.* 2018). The resolvent analysis for viscoelastic pipe flow considering the white noise forcing has found that the most strongly amplified resolvent mode exhibits thin tilted sheets like fluctuations in the polymeric stress field at the critical layer (Zhang 2021), which closely resembles the structure of the most dominant travelling wave discovered here using the VESPOD analysis, suggesting a possible connection of the dominant coherent structures underlying EIT in pipe flow with its linear dynamics. For channel flow, it has already been demonstrated that the TS mode resulting from the linear stability analysis closely resembles the most strongly amplified resolvent mode (Shekar *et al.* 2019) and the most dominant SPOD mode underlying EIT (Kumar & Graham 2024).

The differences between the velocity fields of the dominant travelling waves underlying EIT in channel and pipe flows result at least in part from the differences in their underlying Newtonian linear stability problems and symmetries imposed for 2-D dynamics. The linear instability of a wall mode leads to the emergence of the TS wave in Newtonian channel flow, which sets the structure and symmetry (shift-reflect) of the most dominant travelling wave underlying EIT in channel flow. In contrast, no analogous wall mode linear instability arises in pipe flow. Additionally, the constraint that the wall-normal velocity has to vanish at the axis for an axisymmetric flow precludes the shift-reflect symmetry of the TS wave for travelling waves underlying EIT in pipe flow. However, the common critical layer mechanism responsible for the formation of thin sheets in the polymeric stress field can explain the similarities observed in the structures of the polymeric stress field of the dominant travelling waves underlying EIT in both channel and pipe flows.

4. Conclusions

In the present study, we reveal the dominant well-defined structures underlying the dynamics of elastoinertial turbulence (EIT) in axisymmetric pipe flow using a viscoelastic variant of spectral proper orthogonal decomposition (VESPOD). The VESPOD enables

https://doi.org/10.1017/jfm.2026.11909 Published online by Cambridge University Press

us to perform modal decomposition of velocity and polymeric stress fields together, and identify coherently evolving mode structures that contribute the most to the total mechanical energy of the dynamics of EIT. The leading eigenvalue of the VESPOD spectrum contains most of the mechanical energy and hence dominates its dynamics. The leading eigenvalue of the VESPOD energy spectrum of each wavenumber (κ) structure exhibits three distinct peaks. Further analysis of the mode structures corresponding to these peaks reveals three distinct families of well-defined travelling waves, which are characterised by their wave speed, and dominate the dynamics of EIT in axisymmetric pipe flow. The higher wavenumber structures ($\kappa \geqslant 2$) of each family of travelling waves are harmonics of their respective fundamental waves ($\kappa = 1$). The radial velocity component of these travelling waves contains large-scale structures spanning the radial direction; however, the polymeric stress field contains thin sheets of high stress fluctuations localised at the critical layers of the travelling waves. The critical layers contain hyperbolic stagnation points (in the reference frame moving with the wave speeds), which lead to the emergence of thin polymeric sheets. The substantial portion of fluctuations in EIT travel downstream with the three wave speeds as the form of highly coherent travelling wave structures, and the radial positions corresponding to their critical layers are the preferred locations for the formation of thin sheets in the polymeric stress field. Further, the polymeric sheets of a given travelling wave confine the polymeric sheets of immediately faster waves, leading to a nested arrangement of the polymeric sheets. At larger values of the Reynolds numbers and Weissenberg numbers, the EIT dynamics becomes more chaotic, leading to the emergence of non-harmonic travelling waves, along with the three families of harmonic travelling waves, having energy content comparable to the harmonic waves.

Supplementary movies. Supplementary movies are available at https://doi.org/10.1017/jfm.2026.11909.

Funding. This research was supported under Office of Naval Research grant N00014-18-1-2865 (Vannevar Bush Faculty Fellowship) and National Science Foundation grant CBET-2437151.

Declaration of interests. The authors report no conflict of interest.

Appendix A. Validation of numerical tool

We use the method of the manufactured solution for the validation of the numerical tool. We assume a solution having velocity and conformation tensor fields

$$u_z = (1 - r^2)\sin(z), \quad u_r = 0, \tag{A1}$$

and

$$\boldsymbol{\alpha} = (1 + \sin(z))\boldsymbol{I}. \tag{A2}$$

Next, we analytically obtain forcing functions to the governing equations (2.1) and (2.3) that satisfy the assumed solution (A1)–(A2). Using these forcing terms, we perform a numerical simulation, and find good agreement between the computed solution and the analytical solution (figure 14).

Appendix B. Mesh resolution and *Sc* dependency of solution

To illustrate the impact of mesh resolution and *Sc* on the EIT result, we depict the snapshots of the zz-component of the polymeric stress field (as this component is the most sensitive) obtained using different *Sc* values and the respective mesh resolution and

https://doi.org/10.1017/jfm.2026.11909 Published online by Cambridge University Press

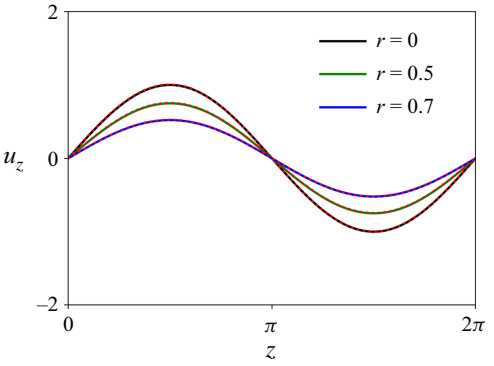


Figure 14. Exact (solid lines) and computed (dotted lines) profiles of u_z for a manufactured solution of viscoelastic flow through an axisymmetric pipe at $Re = 3000$, $Wi = 35$, $\beta = 0.97$ and $b = 6400$ (mesh resolution 256×512).

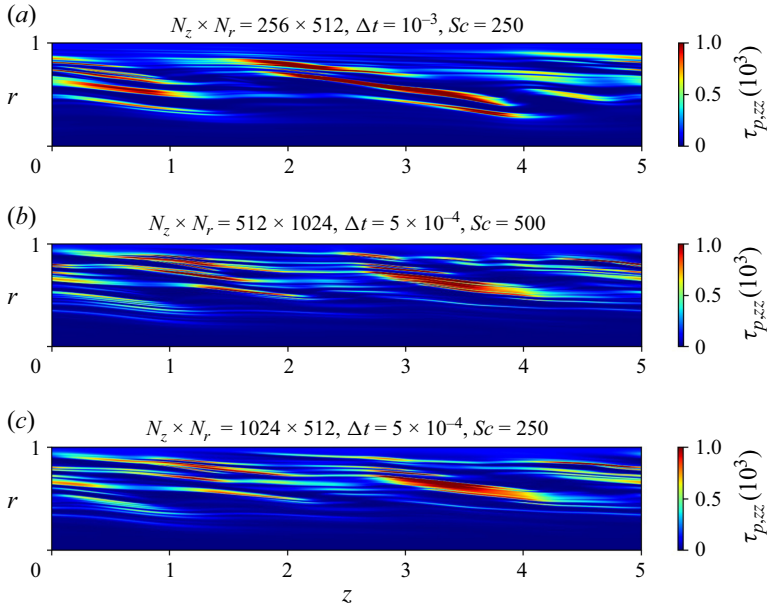


Figure 15. Snapshots of the zz-component of the polymeric stress field for EIT in an axisymmetric pipe flow obtained using different mesh resolutions and Sc at the physical parameter values $Re = 3000$, $Wi = 35$ and $L = 5$.

time step required to successfully evolve the EIT dynamics in axisymmetric pipe flow (figure 15). As the value of Sc increases, polymeric stress diffusion becomes weaker, hence we see the emergence of even finer/sharper filaments oriented along the streamwise direction. The computation at higher Sc becomes significantly expensive due to the requirement of higher mesh resolution and a smaller time step to successfully evolve the dynamics. However, it does not fundamentally change the essential features of EIT and hence the central conclusion of the study. Therefore, in the present study, we use $Sc = 250$, $N_z \times N_r = 256 \times 512$ and $\Delta t = 0.001$, as these simulation parameters provide a reasonable balance between accuracy and computational cost.

https://doi.org/10.1017/jfm.2026.11909 Published online by Cambridge University Press

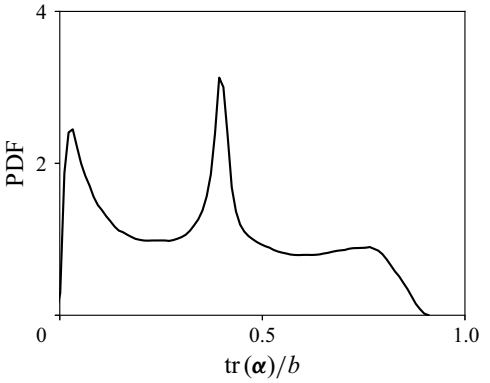


Figure 16. The PDF of $\mathrm{tr}(\boldsymbol{\alpha})/b$ for polymeric stress field in EIT at $Re = 3000$, $Wi = 35$, $\beta = 0.97$ and $b = 6400$.

Appendix C. The PDF of $\mathrm{tr}(\boldsymbol{\alpha})/b$

To estimate the deviation of mechanical energy from the exact value due to the finite b for the inner product used in the present study (2.7), we estimate the PDF of $\mathrm{tr}(\boldsymbol{\alpha})/b$ for the ensemble of polymeric stress field in EIT. We define the PDF as

$$\mathrm{PDF}(\tilde{p}) = \lim_{t\to\infty} \frac{\int_0^t \int_0^L \int_0^1 \delta(p(t,z,r) - \tilde{p}) r \,\mathrm{d}r \,\mathrm{d}z \,\mathrm{d}t}{\int_0^t \int_0^L \int_0^1 r \,\mathrm{d}r \,\mathrm{d}z \,\mathrm{d}t}, \tag{C1}$$

where $p = \mathrm{tr}(\boldsymbol{\alpha})/b$, $\tilde{p}$ is the value of p at which the PDF is evaluated, and δ is the Dirac delta function. Although the maximum value of $\mathrm{tr}(\boldsymbol{\alpha})/b$ is ≈ 0.9, the probability of a high value of $\mathrm{tr}(\boldsymbol{\alpha})/b$ is small (figure 16). In fact, the peaks in the PDF are at approximately $\tilde{p} = 0$ and $\tilde{p} = 0.4$, suggesting that the inner product used in the present study is a good representative of the mechanical energy. Regardless of whether the inner product used in present study exactly captures the mechanical energy, it is an appropriate and physically motivated inner product and norm.

Appendix D. The VESPOD spectra based on different frequency resolutions

For wavenumber $\kappa = 1$ structures, the difference between the consecutive peak frequencies is small, therefore a higher frequency resolution is required to properly resolve the dominant peaks in the VESPOD spectra. We have plotted the leading VESPOD eigenvalue spectra for $\kappa = 1$ structures obtained using different frequency resolutions (figure 17). The frequency resolution $\Delta f = 0.02$ is too coarse to resolve all the peaks associated with $\kappa = 1$ structures, whereas $\Delta f = 0.005$ requires a larger dataset for statistical convergence, and also generates some additional peaks resolving weak variability within broadband structures. Therefore, we choose $\Delta f = 0.01$ for $\kappa = 1$ structures to balance frequency resolution and statistical convergence, enabling clearer identification of the dominant energetic structures.

https://doi.org/10.1017/jfm.2026.11909 Published online by Cambridge University Press

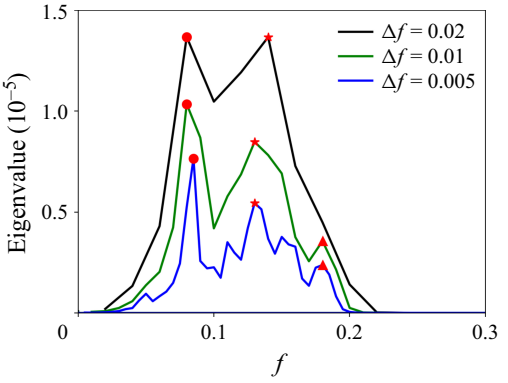


Figure 17. Leading eigenvalues of VESPOD spectra of $\kappa = 1$ structures obtained using different frequency resolutions at $Re = 3000$, $Wi = 35$ and $L = 5$. A total of 24 000 snapshots were used for the frequency resolutions $\Delta f = 0.02$ and $\Delta f = 0.01$, whereas 36 000 snapshots were used for $\Delta f = 0.005$ to maintain statistical convergence.

References

Beneitez, M., Page, J., Dubief, Y. & Kerswell, R.R. 2024*a* Multistability of elasto-inertial two-dimensional channel flow. *J. Fluid Mech.* **981**, A30.

Beneitez, M., Page, J., Dubief, Y. & Kerswell, R.R. 2024*b* Transition route to elastic and elasto-inertial turbulence in polymer channel flows. *Phys. Rev. Fluids* **9** (12), 123302.

Bird, R.B., Curtiss, C.F., Armstrong, R.C. & Hassager, O. 1987 *Dynamics of Polymeric Liquids, Volume 2: Kinetic Theory*. Wiley.

Burns, K.J., Vasil, G.M., Oishi, J.S., Lecoanet, D. & Brown, B.P. 2020 Dedalus: a flexible framework for numerical simulations with spectral methods. *Phys. Rev. Res.* **2** (2), 023068.

Chaudhary, I., Garg, P., Subramanian, G. & Shankar, V. 2021 Linear instability of viscoelastic pipe flow. *J. Fluid Mech.* **908**, A11.

Choueiri, G.H., Lopez, J.M., Varshney, A., Sankar, S. & Hof, B. 2021 Experimental observation of the origin and structure of elastoinertial turbulence. *Proc. Natl Acad. Sci. USA* **118** (45), 1–5.

Datta, S.S. *et al.* 2022 Perspectives on viscoelastic flow instabilities and elastic turbulence. *Phys. Rev. Fluids* **7** (8), 080701.

Drazin, P.G. & Reid, W.H. 1981 *Hydrodynamic Stability*. Cambridge University Press.

Dubief, Y., Page, J., Kerswell, R.R., Terrapon, V.E. & Steinberg, V. 2022 First coherent structure in elasto-inertial turbulence. *Phys. Rev. Fluids* **7** (7), 073301.

Dubief, Y., Terrapon, V.E. & Hof, B. 2023 Elasto-inertial turbulence. *Annu. Rev. Fluid Mech.* **55** (1), 675–705.

Garg, P., Chaudhary, I., Khalid, M., Shankar, V. & Subramanian, G. 2018 Viscoelastic pipe flow is linearly unstable. *Phys. Rev. Lett.* **121** (2), 24502.

Holmes, P., Lumley, J.L., Berkooz, G. & Rowley, C.W. 2012 *Turbulence, Coherent Structures, Dynamical Systems and Symmetry*, 2nd edn. Cambridge Monographs on Mechanics. Cambridge University Press.

Khalid, M., Chaudhary, I., Garg, P., Shankar, V. & Subramanian, G. 2021 The centre-mode instability of viscoelastic plane Poiseuille flow. *J. Fluid Mech.* **915**, A43.

Kumar, M., Constante-Amores, C.R. & Graham, M.D. 2025 Elastoinertial turbulence: data-driven reduced-order model based on manifold dynamics. *J. Fluid Mech.* **1007**, R1.

Kumar, M. & Graham, M.D. 2024 Nested travelling wave structures in elastoinertial turbulence. *J. Fluid Mech.* **993**, A8.

Kumar, M., Guasto, J.S. & Ardekani, A.M. 2023 Lagrangian stretching reveals stress topology in viscoelastic flows. *Proc. Natl Acad. Sci. USA* **120** (5), e2211347120.

Lewy, T. & Kerswell, R.R. 2025 Revisiting two-dimensional viscoelastic Kolmogorov flow: a centre-mode-driven transition. *J. Fluid Mech.* **1007**, A55.

Lopez, J.M., Choueiri, G.H. & Hof, B. 2019 Dynamics of viscoelastic pipe flow at low Reynolds numbers in the maximum drag reduction limit. *J. Fluid Mech.* **874**, 699–719.

https://doi.org/10.1017/jfm.2026.11909 Published online by Cambridge University Press

MOROZOV, A. 2022 Coherent structures in plane channel flow of dilute polymer solutions with vanishing inertia. *Phys. Rev. Lett.* **129** (1), 017801.

PAGE, J., DUBIEF, Y. & KERSWELL, R.R. 2020 Exact traveling wave solutions in viscoelastic channel flow. *Phys. Rev. Lett.* **125** (15), 154501.

SAMANTA, D., DUBIEF, Y., HOLZNER, M., SCHÄFER, C., MOROZOV, A.N., WAGNER, C. & HOF, B. 2013 Elasto-inertial turbulence. *Proc. Natl Acad. Sci. USA* **110** (26), 10557–10562.

SCHMIDT, O.T. 2022 Spectral proper orthogonal decomposition using multitaper estimates. *Theor. Comput. Fluid Dyn.* **36** (5), 741–754.

SHEKAR, A., MCMULLEN, R.M., MCKEON, B.J. & GRAHAM, M.D. 2020 Self-sustained elastoinertial Tollmien–Schlichting waves. *J. Fluid Mech.* **897**, A3.

SHEKAR, A., MCMULLEN, R.M., MCKEON, B.J. & GRAHAM, M.D. 2021 Tollmien–Schlichting route to elastoinertial turbulence in channel flow. *Phys. Rev. Fluids* **6** (9), 093301.

SHEKAR, A., MCMULLEN, R.M., WANG, S., MCKEON, B.J. & GRAHAM, M.D. 2019 Critical-layer structures and mechanisms in elastoinertial turbulence. *Phys. Rev. Lett.* **122** (12), 124503.

SID, S., TERRAPON, V.E. & DUBIEF, Y. 2018 Two-dimensional dynamics of elasto-inertial turbulence and its role in polymer drag reduction. *Phys. Rev. Fluids* **3** (1), 011301.

TOMS, B.A. 1949 Some observations on the flow of linear polymersolutions through straight tubes at large Reynolds numbers, *Proc. 1st Intl Congr. Rheol*, 135–141, **2**

TOWNE, A., SCHMIDT, O.T. & COLONIUS, T. 2018 Spectral proper orthogonal decomposition and its relationship to dynamic mode decomposition and resolvent analysis. *J. Fluid Mech.* **847**, 821–867.

VIRK, P.S., MICKLEY, H.S. & SMITH, K.A. 1970 The ultimate asymptote and mean flow structure in Toms' phenomenon. *J. Appl. Mech.* **37** (2), 488–493.

WAN, D., SUN, G. & ZHANG, M. 2021 Subcritical and supercritical bifurcations in axisymmetric viscoelastic pipe flows. *J. Fluid Mech.* **929**, A16.

WANG, S., GRAHAM, M.D., HAHN, F.J. & XI, L. 2014 Time-series and extended Karhunen–Loève analysis of turbulent drag reduction in polymer solutions. *AIChE J.* **60** (4), 1460–1475.

WELCH, P. 1967 The use of fast Fourier transform for the estimation of power spectra: a method based on time averaging over short, modified periodograms. *IEEE Trans. Audio Electroacoust.* **15** (2), 70–73.

XI, L. 2019 Turbulent drag reduction by polymer additives: fundamentals and recent advances. *Phys. Fluids* **31**, 121302.

ZHANG, M. 2021 Energy growth in subcritical viscoelastic pipe flows. *J. Non-Newtonian Fluid Mech.* **294**, 104581.

ZHANG, M., LASHGARI, I., ZAKI, T.A. & BRANDT, L. 2013 Linear stability analysis of channel flow of viscoelastic Oldroyd-B and FENE-P fluids. *J. Fluid Mech.* **737**, 249–279.

https://doi.org/10.1017/jfm.2026.11909 Published online by Cambridge University Press